

X-Ray Polarization from the Gamma-Ray Binary LS I +61° 303

PHILIP KAARET ¹, SUDIP CHAKRABORTY ², DANIEL GOLONKA ², OLIVER J. ROBERTS ^{2,3}, IOANNIS LIODAKIS ⁴,
ANDREA GNARINI ¹, STEVEN R. EHLERT ¹ AND JOEL B. COLEY ^{5,6}

¹NASA Marshall Space Flight Center, Huntsville, AL 35812, USA

²Science and Technology Institute, Universities Space and Research Association, Huntsville, AL 35805, USA

³School of Physics, University Road, University of Galway, Galway, Ireland, H91 TK33

⁴Institute of Astrophysics, Foundation for Research and Technology-Hellas, GR-70013 Heraklion, Greece

⁵Department of Physics and Astronomy, Howard University, Washington, DC 20059, USA

⁶CRESST and NASA Goddard Space Flight Center, Astrophysics Science Division, 8800 Greenbelt Road, Greenbelt, MD

ABSTRACT

The gamma-ray emitting binary stellar system LS I +61° 303 was observed with the Imaging X-ray Polarimetry Explorer (IXPE) on two successive orbits over orbital phases of 0.74 to 1.05. Polarization is detected at a significance of 4.2σ with an average polarization degree of $13.1\% \pm 3.0\%$ in the 2–8 keV band after background subtraction. This is the second detection of polarization of the X-ray synchrotron emission from a gamma-ray binary and, again, suggests that the magnetic field in the particle acceleration region has a significant ordered component. The orbital motion on the sky of LS I +61° 303 is not well determined, which leads to ambiguity in interpretation of the X-ray electric vector polarization angle (EVPA) measurement. Use of orbital elements determined via radial velocity measurements combined with radio imaging of variable nebular emission, suggests an offset between the X-ray EVPA and the compact object-massive star axis on the order of $\sim 30^\circ$. Such an offset could be produced by Coriolis forces due to binary motion. Use of two different sets orbital elements determined via optical polarimetry suggest either no offset or a perpendicular orientation, but require an unexpectedly high inclination. Use of orbital elements derived from modeling of the keV/TeV light curves suggest good alignment between the X-ray EVPA and the compact object-massive star axis. Such alignment was found for the gamma-ray binary PSR B1259-63. If the same physical situation holds for LS I +61° 303, that would favor the orbital elements derived from the keV/TeV light curves.

1. INTRODUCTION

Gamma-ray binaries are stellar binary systems emitting radiation at energies above 100 MeV and containing a compact object and a massive star (Dubus 2013). The high energy radiation indicates the presence of highly relativistic particles. Radio pulsations on timescales of ms have been found in three gamma-ray binaries confirming that the compact object is a rapidly spinning neutron star: PSR B1259-63 (Johnston et al. 1994), PSR J2032+4127 (Camilo et al. 2009), and LS I +61° 303 (Weng et al. 2022).

The intrabinary shock formed where the relativistic outflow from a rapidly-rotating neutron star interacts with the wind from a massive star is a natural site for acceleration of particles to highly relativistic energies. The X-ray emission is then synchrotron radiation from these particles moving in the magnetic fields in or near the acceleration region (Tavani & Arons 1997). X-ray polarization can be a useful tool to probe the magnetic field configuration near the acceleration region.

The first such observations were made of the gamma-ray binary PSR B1259–63 using the Imaging X-Ray Polarimetry Explorer (IXPE; Weisskopf et al. 2022) during an X-ray bright phase shortly after its periastron passage on 2024 June 30 (Kaaret et al. 2024). X-ray polarization was detected with a polarization degree of $8.3 \pm 1.5\%$ at a significance of 5.3σ . The X-ray polarization angle was found to be aligned with the shock cone axis at the time of the observation, indicating the predominant component of the magnetic field in the acceleration region was oriented perpendicular to the shock cone axis. Measurements of other TeV binaries are needed to determine whether this magnetic field geometry is common for these kind of sources. The results can be used to advance our understanding of relativistic shock acceleration.

Here, we present the results of IXPE observations of the gamma-ray binary LS I +61° 303, hereafter LS61. We discuss some details of the binary in section 2, the IXPE observations in section 3, and the results in section 4. We conclude, in section 5, with some discussion of the implications of the results.

2. TEV BINARY LS I +61 303

LS61 is a gamma-ray binary located at a distance of 2.65 ± 0.09 kpc (Lindgren et al. 2021) and comprises a compact object in an eccentric orbit around a rapidly-rotating B0Ve star with an orbital period of 26.4960 ± 0.0028 d and a superorbital period of 1667 ± 8 d (Gregory 2002). The best determinations of the periods are from long-term radio monitoring. The zero of the orbital phase of the compact object is set for historical reasons at MJD 43366.275 (Gregory 2002).

The gamma-ray source 2CG 135+01 was discovered by the COS B satellite in a survey of the Galactic plane at energies above 100 MeV (Hermsen et al. 1977). In 2006, the MAGIC telescope provided greatly improved localization of the gamma-ray emission, confirming the long suspected identification with the optical and radio source LS I +61° 303 (Albert et al. 2006). MAGIC also detected variable TeV gamma-ray emission modulated by the orbital period, which was confirmed by VERITAS observations (Acciari et al. 2008), with both instruments detecting enhanced TeV emission over orbital phases of 0.6 to 0.8. LS61 has also been observed to produce bright TeV flares with rise and fall times of less than a day (Archambault et al. 2016). Flares in the X-ray band are even faster with doubling times as fast as 2 s (Smith et al. 2009). The X-ray emission also shows a strong correlation between the flux and photon index, with the spectrum becoming harder at higher fluxes (Smith et al. 2009; Li et al. 2011). Recently, ultra-high energy emission (>100 TeV) was reported by the Large High Altitude Air Shower Observatory (LHASSO) with significances of 9.2σ in the Water Cherenkov Detector Array (WCDA; 1.4–30.5 TeV) and 6.2σ in the Kilometer Square Array (KM2A; 25–267 TeV) (Cao et al. 2026). The short time scales of X-ray (Smith et al. 2009; Torres et al. 2012) and TeV flaring (Archambault et al. 2016) suggests that particle acceleration can occur on short time scales, while the detection at ultra-high energies requires acceleration to ultra-high energies.

Very Long Baseline Interferometry (VLBI) radio imaging reveals that the emission from LS61 is extended on scales of milliarcseconds with time variable position and morphology. The position of the radio emission peak moves in an elliptical pattern as a function of orbital phase (Dhawan et al. 2006; Wu et al. 2018). However, the ellipse is much larger (semimajor axis ≈ 1.6 mas) than the optically-measured orbit size (semimajor axis ≈ 0.2 mas).

The nature of the compact object, either neutron star or black hole, in LS61 has long been debated. While the non-thermal emission from LS 61 was postulated soon after discovery to possibly come from a millisecond pulsar (Maraschi & Treves 1981), dedicated searches using the entire archive of Rossi X-ray Timing Explorer Proportional Counter Array (PCA) data revealed no pulsations (López-Miralles et al. 2023). Tor-

res et al. (2012) reported a singular, short (0.24 s) X-ray burst they described as ‘magnetar-like’ detected by the Swift Burst Alert Telescope and likely originating from LS61 which would suggest the compact object is a highly magnetized neutron star. Recent observations with the Five-hundred-meter Aperture Spherical radio Telescope (FAST) suggest that the compact object is a rotationally-powered NS with a period of 269.15508 ± 0.00016 ms (Weng et al. 2022). The FAST results are not fully conclusive because the field of view is too large to definitively rule out an interloper and no Doppler shift was detected as might be expected for a pulsar in a binary system (Jaron et al. 2024). However, the high significance of the pulsed signal ($> 20\sigma$), the lack of accretion signatures such as disk emission, and the identification of pulsars in other gamma-ray binaries with larger orbital separation lead us to conclude the compact object in LS61 is most likely a neutron star.

In this case, the particle acceleration likely occurs at the intrabinary shock formed where the relativistic wind from the neutron star interacts with the equatorial wind from the Be-star (Maraschi & Treves 1981). Also, the extended radio emission is likely synchrotron emission from particles accelerated in the same shock (Dhawan et al. 2006).

2.1. Orbital elements

Knowledge of the position angle on the sky of the compact object relative to the binary system center of mass is needed to interpret the X-ray polarization angle. The orbit of PSR B1259–63 was measured via highly accurate radio timing and astrometric observations of the pulsed emission which is detected over most of the orbit, except close to periastron (Miller-Jones et al. 2018). This provided direct measurement of the position of the pulsar itself. In contrast, pulsed emission from LS61 has been detected only in a single, 3-hr observation. Thus, no direct measurement of the orbital motion of the pulsar on the sky is available. Orbital information on LS61 is available from several different techniques: radial velocity measurements, optical polarimetry, and modeling of the high energy emission.

The most common are radial velocity measurements (Hutchings & Crampton 1981; Casares et al. 2005; Grundstrom et al. 2007; Aragona et al. 2009). These provide the mass function ($f(M)$), eccentricity (e), and phase (ϕ_P) and argument (ω) of periastron. However, the optical line profiles are not purely from the atmosphere of the Be star, as assumed for radial velocity measurement, but may have contributions from the disk or gaseous shell surrounding the star. This requires careful selection of (relatively) uncontaminated absorption line features. Even so, the radial velocity measurements tend to exhibit large scatter around the best-fitted curve. Also, different solutions are found depending on the data set used, e.g. the eccentricity varies from 0.34 ± 0.08 to 0.72 ± 0.15 (Grundstrom et al. 2007; Casares et al. 2005).

Radial velocity measurements do not provide the orbital inclination (i) and longitude of ascending node (Ω) which is associated with the orientation of the orbital major axis on the sky. The mass function, $f = M_{\odot} = (M_2 \sin i)^3 / (M_1 + M_2)^2$ can be used to place some constraints on i . We use the mass function of $f = 0.0124 \pm 0.0022$ from [Aragona et al. \(2009\)](#) and assume the compact object is a neutron star with $M_2 = 1.35M_{\odot}$ ([Özel & Freire 2016](#)). For a nominal B0Ve star mass of $M_1 = 12.5M_{\odot}$, the inclination is then $i = 75^{\circ}$. We use this value below for orbital solutions that do not determine the inclination. The inclination increases with increasing M_1 and reaches $i = 90^{\circ}$ for Be star mass $M_1 \lesssim 13M_{\odot}$. For Be star masses at the low end of the allowed range, $M_1 = 10M_{\odot}$ ([Casares et al. 2005](#)), then $i = 40^{\circ}$. [Hutchings & Crampton \(1981\)](#) reported detection of ‘shell features’ that are seen when the Be star is viewed through its disk and suggest that $\sin i$ is close to 1 under the assumption that Be disk is coplanar with the orbit. However, [Casares et al. \(2005\)](#) report a lack of clear shell lines and suggest that $i \lesssim 60^{\circ}$. The absence of X-ray eclipses would favor lower inclinations, $i \lesssim 60^{\circ}$, if the X-ray emission is confined to near the compact object.

To derive Ω , we assume that ellipse traced by the radio emission peak is aligned with the binary orbit. [Wu et al. \(2018\)](#) derive a position angle (PA) of $\theta_{\text{obs}} \approx -43.6^{\circ} \pm 1.6^{\circ}$ East of North for the radio peak ellipse. Converting this to the standard $0^{\circ} - 180^{\circ}$ convention for the line of nodes yields a position angle for the major axis of $\theta = 136.4^{\circ}$. The apparent orientation of the projected semi-major axis on the sky (θ) is related to Ω , i , and ω through the 3D projection of the periastron vector onto the sky plane. In Appendix A, we show that the longitude of the ascending node is $\Omega = \theta - \arctan(\tan \omega \cos i)$. Thus, given values i and ω , we can calculate the Ω from the [Wu et al. \(2018\)](#) estimation of θ .

[Kravtsov et al. \(2020\)](#) use a fundamentally different technique, high-precision optical photo-polarimetry, to derive the orbital elements of LS61. Because polarimetry provides geometric information, the measurements do accurately constrain the orientation of the orbit on the sky and, thus, use of the VLBI imaging is not needed. Optical polarimetry is nominally sensitive to the orbital inclination. However, the inclination results are biased towards high values in the presence of instrumental or intrinsic noise as described further below.

The time-dependent high energy emission observed from gamma-ray binaries is strongly influenced by the orbital geometry. [Chen & Takata \(2022\)](#) developed a model for the emission (X-ray synchrotron and gamma-ray inverse Compton) produced by particles accelerated at the intrabinary shock in binaries containing a pulsar orbiting a Be star. They used the model to estimate the orbital elements for LS61 via fits to the observed X-ray and gamma-ray light curves. The light curves do not

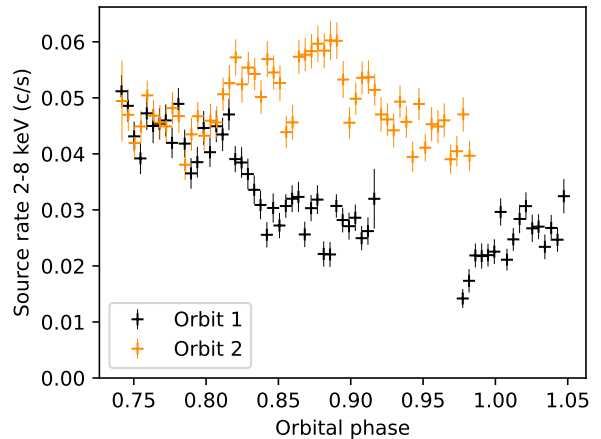


Figure 1. IXPE count rate in the 2-8 keV band versus orbital phase. Black points are observations during the first orbit, while orange points are during the second orbit.

include geometric information. Thus, we need to add an assumed i and calculate Ω from the VLBI imaging, as for the radial velocity orbital solutions.

3. IXPE OBSERVATIONS AND REDUCTION

IXPE observed LS61 in three segments from 14 Feb 2026 (MJD 61085.250) to 19 Mar 2026 (MJD 61118.217). IXPE has three X-ray telescopes, each containing a Mirror Module Assembly ([Ramsey et al. 2022](#), MMA) and a detector unit (DU) housing a gas pixel detector (GPD) sensitive to linear X-ray polarization ([Soffitta et al. 2021](#); [Baldini et al. 2021](#)). We analyze data from all three DUs. We removed background flares by filtering on 2-8 keV band counting rates extracted from a background region with inner radius of $2.5'$ and outer radius of $5.0'$, excising intervals when summed count rate in the three DUs in a 240 s time bin exceeded the mean rate by more than 3 times the standard error on the rate measurement. After filtering, the total exposure was 713.9, 713.7, and 714.0 ks for DU1, DU2, and DU3, respectively.

We extracted source counts from a circular region with a radius of $60''$. The source region was centered visually using the IXPE images; the best centroid was $7.5''$ from the nominal source location. We extracted background counts from a concentric annulus with radii of $150''$ and $300''$ ([Di Marco et al. 2023](#)). The source spectrum is above the background spectrum, scaled for the region sizes, in the full IXPE 2-8 keV band. Hence, we use that energy band for subsequent analysis. The data were processed with CALDB version 20260331 and HEASoft version 6.36 was used in the analysis.

4. RESULTS

The IXPE observations cover portions of two orbits of LS61. Figure 1 shows the IXPE count rate in the 2-8 keV band versus orbital phase. The time bins are 10^4 s and the rate is summed over the 3 DUs. The

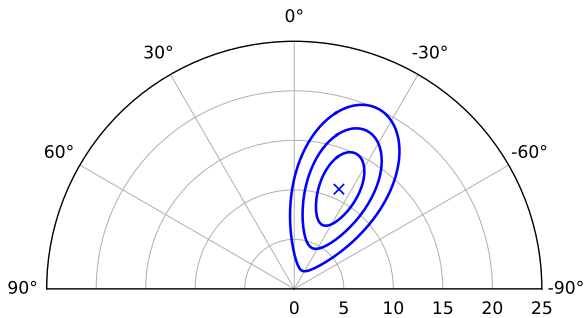


Figure 2. Contour plots of the polarization degree and angle without correction for background. The \times marks the measured values. The contours show the 68.27%, 95.45%, and 99.73% confidence intervals for χ^2 on 2 degrees of freedom. Position angles are measured positive east of north.

phase coverage was planned to match times when the X-ray flux is brighter and TeV emission has historically been observed (Smith et al. 2009). The flux was notably higher during the second orbit.

For our initial polarization analysis, we performed a model-independent calculation in the 2-8 keV band using counts from the source region for the full observation. Each event was weighted based on how well the electron track could be used to correctly reconstruct the original photoelectron direction. No correction was made for background. Figure 2 shows the average polarization of the source events. The plot was produced with the `ixpe_protractor.py` script on the IXPE User Contributed software page, which uses the `ixpepolarization` tool in HEASoft. The polarization results from the individual DUs are all consistent with the summed result within the 68% confidence contour.

The observed polarization degree (PD) is $11.0\% \pm 2.6\%$. All uncertainties are reported at 68.27% confidence. The detection is significant at the 4.2σ confidence level and indicates a secure detection of X-ray polarization. The electric vector position angle (EVPA) is $-24^\circ.1 \pm 6^\circ.8$ and is measured anticlockwise from north in the equatorial coordinate system. We found no significant polarization for the background region. Correcting for background utilizing the additive nature of the Stokes parameters, we estimate the PD of the source as $13.1\% \pm 3.0\%$ and the EVPA as $-23^\circ.8 \pm 6^\circ.6$. The EVPA is consistent with that found without background subtraction. The source region contained 33284 counts, of which we estimate 4258 are due to background. Due to the relatively low background fraction, we did not attempt to reduce the instrumental background using the rejection algorithm described in Di Marco et al. (2023).

Motivated by the change in flux between the two orbits, we found the polarization for each orbit. We find no statistically significant difference. For the first orbit, $PD = 11.2\% \pm 4.0\%$, and for the second orbit, $PD = 11.1\% \pm 3.5\%$. The EVPA is consistent between the two orbits and with the observation average. We

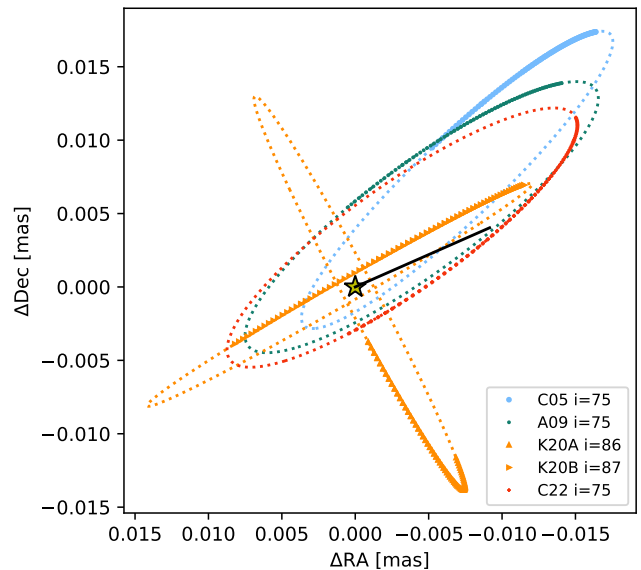


Figure 3. Orbital motion of LS61 on the sky. Shown is the orbital motion of LS61 for the orbital solution of Casares (C05, blue), Aragona (A09, green), and Chen (C22, orange) for $i = 60^\circ$ and the orbital solution of Kravtsov (K20, vermillion). The star shows the system barycenter. The black line segment emanating from the star indicates the X-ray EVPA. The points mark the times of the IXPE light curve segments shown in Fig. 1.

also divided the observation into two intervals by flux; there was no significant difference in PD.

We performed a spectropolarimetric analysis. We generated I, Q, and U spectra in the 2-8 keV band and response files for each DU using `ixpeproduct` in HEASoft. The same source and background regions described above were used. The Stokes I spectra were binned to have 80 eV bins below 3 keV and 120 eV above. The Stokes Q and U spectra were binned with 400 eV bins. We modeled the spectrum using an absorbed power law with constant polarization multiplied by a constant allowed to vary between the three DUs. The column density for the `phabs` absorption model was fixed to $0.5 \times 10^{22} \text{ cm}^{-2}$ (Chernyakova et al. 2017) using abundances from Anders & Grevesse (1989) and cross-sections from Verner et al. (1996). We obtained a good fit with $\chi^2/\text{DoF} = 238.6/240$. We found $PD = 11.4\% \pm 2.8\%$ and $EVPA = -24^\circ.1 \pm 7^\circ.1$. Both are consistent with the background-subtracted model-independent results. We found a photon index of $\Gamma = 1.46 \pm 0.03$ within the range measured previously in the 2-10 keV band (Smith et al. 2009).

5. DISCUSSION

Our IXPE observations have led to the detection of significant X-ray polarization (4.2σ confidence level) from LS61 with a background-subtracted $PD = 13.1\% \pm 3.0\%$. This is the second detection of X-ray polarization

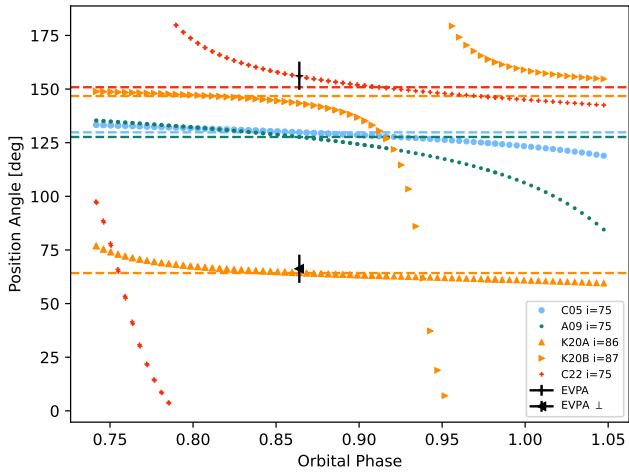


Figure 4. Pulsar position angle versus orbital phase for the IXPE light curve segments. The orbital solutions and inclinations are as in Fig. 3. The dashed horizontal lines indicate the median of each distribution. The points show the X-ray EVPA and rotated by 90° (EVPA_\perp) and are plotted at the median orbital phase of the IXPE light curve segments.

from a TeV binary. The PD is higher than that detected from PSR B1259–63 during an X-ray bright phase following the periastron passage in 2024 June (Kaaret et al. 2024).

The polarization degree (PD) for synchrotron radiation is determined by the particle spectral index and the level of uniformity of the magnetic field. The maximum polarization for LS61 is $\sim 70\%$. The reduction in observed PD relative to the maximum is roughly equal to the ratio of the energy in the uniform magnetic field component to that in the total field (Burn 1966). The observed PD of 13% suggests that $\sim 20\%$ of the magnetic field is in the uniform component. However, the observed PD can also be reduced if the shock-cone axis is not perpendicular to the line of sight (Laing 1980; Xingxing & Jumpei 2021) or due to curvature of the shock in the acceleration region. Thus, the fraction of $\sim 20\%$ of the field in the uniform component should be considered as a lower bound.

The X-ray EVPA for synchrotron radiation is set by the magnetic field orientation in and near the acceleration region. This is set by the shock cone axis which thought to be is aligned with the pulsar orbital position angle on the sky at the time of the observation (Bogovalov et al. 2008). Figure 3 shows the pulsar orbit for LS61 projected on the sky calculated with orbital parameters determined as described in section 2.1. We show orbits using the elements from Casares et al. (2005), Aragona et al. (2009), and Chen & Takata (2022) for which we have taken $i = 75^\circ$ and using the two solutions from Kravtsov et al. (2020) with the fitted inclination indicated in the legend. In the figure, the dotted

curves show the full orbit. The times of the IXPE light curve points shown in Fig. 1 are plotted as points. The star shows the system center of mass with the line segment emanating from it indicating the X-ray EVPA.

The pulsar moves over a range of position angles during the IXPE observations. The position angle versus orbital phase for each light segment is shown in Figure 4. The measured X-ray EVPA of $180 - 23.8 \pm 6.6 = 156.2 \pm 6.6$ is also shown. Remarkably, the EVPA is not aligned with the pulsar position angle during the observation for either the Casares or Aragona orbital elements. The minimum offset between EVPA and median is 26° for the Casares elements with $i = 75^\circ$. The offset for the Aragona elements is 28° . These offsets are significantly larger than the uncertainty in the EVPA. Neither of these two position angle distributions overlap with the measured EVPA allowing for uncertainties. The offset increases for lower i .

In contrast, the offset between the X-ray EVPA and median pulsar position angle during the IXPE observations as calculated using the Kravtsov orbital elements with Ω free (lower part of Table 4, K20B in Figures 3 and 4) is only 10° . The EVPA and median pulsar position angle are consistent within the 90% confidence interval. However, the best fitted inclination is high, $i = 87^\circ \pm 3^\circ$. Polarimetrically-derived inclinations are biased towards high values when noise is present (Simmons et al. 1982). The optical polarization signal from LS61 shows strong intrinsic stochastic variations that drive the fitted inclination to high values, but the 2σ confidence interval extends down to $i = 20^\circ$ (Kravtsov et al. 2020). The pulsar position angle inferred from the Kravtsov orbital elements depends strongly on i , assuming that the other orbital elements remain unchanged if the inclination is varied (Kravtsov, private communication). For $i = 80^\circ$, the offset is as large as for the orbits based on radial velocity measurements.

In contrast, for the Kravtsov orbital elements with Ω constrained (upper part of Table 4, K20A in our figures), the median of the pulsar position angle is perpendicular to the X-ray EVPA within 2° . This orbit is largely perpendicular to the other orbits. Again, the offset increases for smaller i and is as large as for the orbits based on radial velocity measurements for $i = 78^\circ$.

Remarkably, the orbital elements of Chen & Takata (2022) provide a good match to the X-ray EVPA when using $i = 75^\circ$ and the orbital orientation on the sky inferred from the radio imaging. The median pulsar position angle is 151° which is well within the 68% confidence interval for the X-ray EVPA. A good match is also obtained for $i = 60^\circ$, with a median pulsar position angle of 153.7° , only 2.5° from the X-ray EVPA. A large offset of 99° is obtained for $i = 45^\circ$.

For PSR B1259–63, the X-ray polarization angle was found to be well aligned with the pulsar position angle during the IXPE observation (Kaaret et al. 2024). This was interpreted as implying that the axis of the

shock cone, where the high energy particles producing the X-ray synchrotron emission are accelerated, was also aligned with the pulsar-primary axis and, therefore, that the predominant component of the magnetic field in the acceleration region is oriented perpendicular to the shock cone axis. If the same physical situation found for applies to LS61, then the IXPE results would favor the Chen orbit elements.

The Kravtsov orbital elements found with Ω free (K20B) could also provide a good match, however the high orbital inclination appears to be an artifact, thus the match may be spurious. The Kravtsov orbital elements found with Ω constrained lead to a pulsar position angle nearly perpendicular to the X-ray EVPA. This would imply that the magnetic field is parallel to the shock cone axis, orthogonal to the geometry found for PSR B1259–63. Again, the match may be spurious due to the unexpectedly high inclination.

If the orbits derived from radial velocity measurements and radio imaging are correct, then there is a misalignment on the orbit of $\sim 30^\circ$ between the pulsar-primary position angle and the X-ray EVPA. This would suggest that the shock region where particles are ac-

celerated to produce the observed X-ray synchrotron emission is misaligned with the pulsar-primary axis. Bosch-Ramon et al. (2012) have performed relativistic hydrodynamical simulations in two dimensions of the stellar/pulsar-wind interaction accounting for orbital motion. They find that the Coriolis force induced by orbital motion deflects the shocked flows. This causes the shock region to become asymmetric with respect to the pulsar-primary axis. In this case, measurement of the X-ray EVPA would provide a probe into the dynamics of the stellar-pulsar wind interaction.

X-ray polarimetry can provide important, new information on shock acceleration and the pulsar-stellar wind interaction. The X-ray polarization degree observed from LS61 suggests there is a substantial well-ordered component of the magnetic field within or near the shock acceleration region. The observed X-ray polarization angle is related to the pulsar motion projected on the sky and may provide an independent way to break degeneracies and settle debates regarding the true orbit of LS61. If the true orbit can be determined independently, then the X-ray position angle would provide a probe of the intrabinary shock formation.

APPENDIX

A. LONGITUDE OF ASCENDING NODE

The position angle (θ) of the projected major axis is the sum of the longitude of ascending node (Ω) and the apparent, projected argument of periastron (α), $\theta = \Omega + \alpha$. To derive the α , we consider the transformation from the physical orbital plane to the observer's sky plane. We define a coordinate system (x', y', z') in the orbital frame where the x' -axis lies along the Line of Nodes and the orbit lies in the (x', y') plane. The position vector of periastron at a distance r is

$$\vec{v}_{\text{orb}} = \begin{bmatrix} r \cos \omega \\ r \sin \omega \\ 0 \end{bmatrix} \quad (\text{A1})$$

where ω is the argument of periastron. To project this onto the sky plane (x, y), we rotate the system by the inclination i around the Line of Nodes (x' -axis),

$$\begin{bmatrix} x \\ y \\ z \end{bmatrix} = \begin{bmatrix} 1 & 0 & 0 \\ 0 & \cos i & -\sin i \\ 0 & \sin i & \cos i \end{bmatrix} \begin{bmatrix} r \cos \omega \\ r \sin \omega \\ 0 \end{bmatrix} = \begin{bmatrix} r \cos \omega \\ r \sin \omega \cos i \\ r \sin \omega \sin i \end{bmatrix} \quad (\text{A2})$$

The observer on Earth perceives the projection (x, y). The apparent angle α relative to the Line of Nodes (x -axis) is given by

$$\tan \alpha = \frac{y}{x} = \frac{r \sin \omega \cos i}{r \cos \omega} = \tan \omega \cos i \quad (\text{A3})$$

Therefore,

$$\alpha = \arctan(\tan \omega \cos i) \quad (\text{A4})$$

Solving for the longitude of the ascending node, we find

$$\Omega = \theta - \arctan(\tan \omega \cos i). \quad (\text{A5})$$

ACKNOWLEDGMENTS

We thank Vadim Kravtsov for discussion of his optical polarimetry results. OJR acknowledges funding through NASA and Research Ireland Pathway Funding under contract 24/PATH-S/12742(T). AG was supported by an appointment to the NASA Postdoctoral Program at the Marshall Space Flight Center (MSFC), administered by Oak Ridge Associated Universities under contract with NASA. JBC acknowledges support by NASA under award number 80GSFC21M0006. IL was funded by the European Union ERC-2022-STG - BOOTES - 101076343. Views and opinions expressed are however those of the author(s) only and do not necessarily reflect those of the European Union or the European Research Council Executive Agency. Neither the European Union nor the granting authority can be held responsible for them.

The Imaging X-ray Polarimetry Explorer (IXPE) is a joint US and Italian mission. The US contribution is supported by the National Aeronautics and Space Administration (NASA) and led and managed by its Marshall Space Flight Center (MSFC), with industry partner Ball Aerospace (now, BAE Systems). The Italian contribution is supported by the Italian Space Agency (Agenzia Spaziale Italiana, ASI) through contract ASI-OHBI-2022-13-I.0, agreements ASI-INAF-2022-19-HH.0 and ASI-INFN-2017.13-H0, and its Space Science Data Center (SSDC) with agreements ASI-INAF-2022-14-HH.0 and ASI-INFN 2021-43-HH.0, and by the Istituto Nazionale di Astrofisica (INAF) and the Istituto Nazionale di Fisica Nucleare (INFN) in Italy. This research used data products provided by the IXPE Team (MSFC, SSDC, INAF, and INFN) and distributed with additional software tools by the High-Energy Astrophysics Science Archive Research Center (HEASARC), at NASA Goddard Space Flight Center (GSFC).

Facilities: IXPE

Software: HEASOFT (NASA High Energy Astrophysics Science Archive Research Center (HEASARC) 2014), XSPEC (Arnaud 1996), DS9 (Smithsonian Astrophysical Observatory 2000), ASTROPY (Astropy Collaboration et al. 2013, 2018, 2022)

REFERENCES

- Acciari, V. A., Beilicke, M., Blaylock, G., et al. 2008, *The Astrophysical Journal*, 679, 1427, doi: [10.1086/587736](https://doi.org/10.1086/587736)
- Albert, J., Aliu, E., Anderhub, H., et al. 2006, *Science*, 312, 1771, doi: [10.1126/science.1128177](https://doi.org/10.1126/science.1128177)
- Anders, E., & Grevesse, N. 1989, *GeoCoA*, 53, 197, doi: [10.1016/0016-7037\(89\)90286-X](https://doi.org/10.1016/0016-7037(89)90286-X)
- Aragona, C., McSwain, M. V., Grundstrom, E. D., et al. 2009, *ApJ*, 698, 514, doi: [10.1088/0004-637X/698/1/514](https://doi.org/10.1088/0004-637X/698/1/514)
- Archambault, S., Archer, A., Aune, T., et al. 2016, *The Astrophysical Journal Letters*, 817, L7, doi: [10.3847/2041-8205/817/1/L7](https://doi.org/10.3847/2041-8205/817/1/L7)
- Arnaud, K. A. 1996, in *Astronomical Society of the Pacific Conference Series*, Vol. 101, *Astronomical Data Analysis Software and Systems V*, ed. G. H. Jacoby & J. Barnes, 17
- Astropy Collaboration, Robitaille, T. P., Tollerud, E. J., et al. 2013, *A&A*, 558, A33, doi: [10.1051/0004-6361/201322068](https://doi.org/10.1051/0004-6361/201322068)
- Astropy Collaboration, Price-Whelan, A. M., Sipőcz, B. M., et al. 2018, *AJ*, 156, 123, doi: [10.3847/1538-3881/aabc4f](https://doi.org/10.3847/1538-3881/aabc4f)
- Astropy Collaboration, Price-Whelan, A. M., Lim, P. L., et al. 2022, *ApJ*, 935, 167, doi: [10.3847/1538-4357/ac7c74](https://doi.org/10.3847/1538-4357/ac7c74)
- Baldini, L., Barbanera, M., Bellazzini, R., et al. 2021, *Astroparticle Physics*, 133, 102628, doi: [10.1016/j.astropartphys.2021.102628](https://doi.org/10.1016/j.astropartphys.2021.102628)
- Bogovalov, S. V., Khangulyan, D. V., Koldoba, A. V., Ustyugova, G. V., & Aharonian, F. A. 2008, *MNRAS*, 387, 63, doi: [10.1111/j.1365-2966.2008.13226.x](https://doi.org/10.1111/j.1365-2966.2008.13226.x)
- Bosch-Ramon, V., Barkov, M. V., Khangulyan, D., & Perucho, M. 2012, *A&A*, 544, A59, doi: [10.1051/0004-6361/201219251](https://doi.org/10.1051/0004-6361/201219251)
- Burn, B. J. 1966, *MNRAS*, 133, 67, doi: [10.1093/mnras/133.1.67](https://doi.org/10.1093/mnras/133.1.67)
- Camilo, F., Ray, P. S., Ransom, S. M., et al. 2009, *ApJ*, 705, 1, doi: [10.1088/0004-637X/705/1/1](https://doi.org/10.1088/0004-637X/705/1/1)
- Cao, Z., Aharonian, F., Bai, Y. X., et al. 2026, *Phys. Rev. Lett.*, , doi: [10.1103/7xhp-tff7](https://doi.org/10.1103/7xhp-tff7)
- Casares, J., Ribas, I., Paredes, J. M., Martí, J., & Allende Prieto, C. 2005, *MNRAS*, 360, 1105, doi: [10.1111/j.1365-2966.2005.09106.x](https://doi.org/10.1111/j.1365-2966.2005.09106.x)
- Chen, A. M., & Takata, J. 2022, *A&A*, 658, A153, doi: [10.1051/0004-6361/202142258](https://doi.org/10.1051/0004-6361/202142258)
- Chernyakova, M., Babyk, I., Malyshev, D., et al. 2017, *MNRAS*, 470, 1718, doi: [10.1093/mnras/stx1335](https://doi.org/10.1093/mnras/stx1335)
- Dhawan, V., Mioduszewski, A., & Rupen, M. 2006, in *VI Microquasar Workshop: Microquasars and Beyond*, 52.1, doi: [10.22323/1.033.0052](https://doi.org/10.22323/1.033.0052)
- Di Marco, A., Soffitta, P., Costa, E., et al. 2023, *AJ*, 165, 143, doi: [10.3847/1538-3881/acba0f](https://doi.org/10.3847/1538-3881/acba0f)
- Dubus, G. 2013, *A&A Rv*, 21, 64, doi: [10.1007/s00159-013-0064-5](https://doi.org/10.1007/s00159-013-0064-5)

- Gregory, P. C. 2002, *ApJ*, 575, 427, doi: [10.1086/341257](https://doi.org/10.1086/341257)
- Grundstrom, E. D., Caballero-Nieves, S. M., Gies, D. R., et al. 2007, *ApJ*, 656, 437, doi: [10.1086/510509](https://doi.org/10.1086/510509)
- Hermesen, W., Swanenburg, B. N., Bignami, G. F., et al. 1977, *Nature*, 269, 494, doi: [10.1038/269494a0](https://doi.org/10.1038/269494a0)
- Hutchings, J. B., & Crampton, D. 1981, *PASP*, 93, 486, doi: [10.1086/130863](https://doi.org/10.1086/130863)
- Jaron, F., Kiehlmann, S., & Readhead, A. C. S. 2024, *A&A*, 683, A228, doi: [10.1051/0004-6361/202347871](https://doi.org/10.1051/0004-6361/202347871)
- Johnston, S., Manchester, R. N., Lyne, A. G., Nicastro, L., & Spyromilio, J. 1994, *MNRAS*, 268, 430, doi: [10.1093/mnras/268.2.430](https://doi.org/10.1093/mnras/268.2.430)
- Kaaret, P., Roberts, O. J., Ehlert, S. R., et al. 2024, *ApJL*, 974, L1, doi: [10.3847/2041-8213/ad7ba6](https://doi.org/10.3847/2041-8213/ad7ba6)
- Kravtsov, V., Berdyugin, A. V., Piirola, V., et al. 2020, *A&A*, 643, A170, doi: [10.1051/0004-6361/202038745](https://doi.org/10.1051/0004-6361/202038745)
- Laing, R. A. 1980, *MNRAS*, 193, 439, doi: [10.1093/mnras/193.3.439](https://doi.org/10.1093/mnras/193.3.439)
- Li, J., Torres, D. F., Zhang, S., et al. 2011, *ApJ*, 733, 89, doi: [10.1088/0004-637X/733/2/89](https://doi.org/10.1088/0004-637X/733/2/89)
- Lindgren, L., Klioner, S. A., Hernández, J., et al. 2021, *A&A*, 649, A2, doi: [10.1051/0004-6361/202039709](https://doi.org/10.1051/0004-6361/202039709)
- López-Miralles, J., Motta, S. E., Migliari, S., & Jaron, F. 2023, *MNRAS*, 523, 4282, doi: [10.1093/mnras/stad1658](https://doi.org/10.1093/mnras/stad1658)
- Maraschi, L., & Treves, A. 1981, *MNRAS*, 194, 1P, doi: [10.1093/mnras/194.1.1P](https://doi.org/10.1093/mnras/194.1.1P)
- Miller-Jones, J. C. A., Deller, A. T., Shannon, R. M., et al. 2018, *MNRAS*, 479, 4849, doi: [10.1093/mnras/sty1775](https://doi.org/10.1093/mnras/sty1775)
- NASA High Energy Astrophysics Science Archive Research Center (HEASARC). 2014, HEASoft: Unified Release of FTOOLS and XANADU, Astrophysics Source Code Library, record ascl:1408.004. <http://ascl.net/1408.004>
- Özel, F., & Freire, P. 2016, *ARA&A*, 54, 401, doi: [10.1146/annurev-astro-081915-023322](https://doi.org/10.1146/annurev-astro-081915-023322)
- Ramsey, B. D., Bongiorno, S. D., Kolodziejczak, J. J., et al. 2022, *Journal of Astronomical Telescopes, Instruments, and Systems*, 8, 024003, doi: [10.1117/1.JATIS.8.2.024003](https://doi.org/10.1117/1.JATIS.8.2.024003)
- Simmons, J. F. L., Aspin, C., & Brown, J. C. 1982, *MNRAS*, 198, 45, doi: [10.1093/mnras/198.1.45](https://doi.org/10.1093/mnras/198.1.45)
- Smith, A., Kaaret, P., Holder, J., et al. 2009, *ApJ*, 693, 1621, doi: [10.1088/0004-637X/693/2/1621](https://doi.org/10.1088/0004-637X/693/2/1621)
- Smithsonian Astrophysical Observatory. 2000, SAOImage DS9: A utility for displaying astronomical images in the X11 window environment, Astrophysics Source Code Library, record ascl:0003.002. <http://ascl.net/0003.002>
- Soffitta, P., Baldini, L., Bellazzini, R., et al. 2021, *AJ*, 162, 208, doi: [10.3847/1538-3881/ac19b0](https://doi.org/10.3847/1538-3881/ac19b0)
- Tavani, M., & Arons, J. 1997, *ApJ*, 477, 439, doi: [10.1086/303676](https://doi.org/10.1086/303676)
- Torres, D. F., Rea, N., Esposito, P., et al. 2012, *ApJ*, 744, 106, doi: [10.1088/0004-637X/744/2/106](https://doi.org/10.1088/0004-637X/744/2/106)
- Verner, D. A., Ferland, G. J., Korista, K. T., & Yakovlev, D. G. 1996, *ApJ*, 465, 487, doi: [10.1086/177435](https://doi.org/10.1086/177435)
- Weisskopf, M. C., Soffitta, P., Baldini, L., et al. 2022, *Journal of Astronomical Telescopes, Instruments, and Systems*, 8, 026002, doi: [10.1117/1.JATIS.8.2.026002](https://doi.org/10.1117/1.JATIS.8.2.026002)
- Weng, S.-S., Qian, L., Wang, B.-J., et al. 2022, *Nature Astronomy*, 6, 698, doi: [10.1038/s41550-022-01630-1](https://doi.org/10.1038/s41550-022-01630-1)
- Wu, Y. W., Torricelli-Ciamponi, G., Massi, M., et al. 2018, *MNRAS*, 474, 4245, doi: [10.1093/mnras/stx3003](https://doi.org/10.1093/mnras/stx3003)
- Xingxing, H., & Jumpei, T. 2021, *ApJ*, 922, 260, doi: [10.3847/1538-4357/ac273b](https://doi.org/10.3847/1538-4357/ac273b)